npj computational materials

www.nature.com/npjcompumats

ARTICLE OPEN

Persistent half-metallic ferromagnetism in a (111)-oriented manganite superlattice

Fabrizio Cossu[1,2], Heung-Sik Kim[1]✉, Biplab Sanyal[3] and Igor Di Marco[2,3,4]✉

We employ electronic structure calculations to show that a (111)-oriented $(LaMnO_3)_{12}|(SrMnO_3)_6$ superlattice retains a half-metallic ferromagnetic character despite its large thickness. We link this behaviour to the strain and the octahedral connectivity between the layers. This also gives rise to breathing modes, which are coupled to charge and spin oscillations, whose components have a pure e_g character. Most interestingly, the magnetisation reaches its maximum value inside the $LaMnO_3$ region and not at the interface, which is fundamentally different from what observed for the (001) orientation. The inter-atomic exchange coupling shows that the magnetic order arises from the double-exchange mechanism, despite competing interactions inside the $SrMnO_3$ region. Finally, the van Vleck distortions and the spin oscillations are crucially affected by the variation of Hund's exchange and charge doping, which allows us to speculate that our system behaves as a Hund's metal, creating an interesting connection between manganites and nickelates.

npj Computational Materials (2022)8:77 ; https://doi.org/10.1038/s41524-022-00759-x

INTRODUCTION

Due to continuous advances in molecular beam epitaxy[1,2] and pulsed laser deposition[2–8], perovskites (and the more general Ruddlesden-Popper family, $A_{n+1}B_nO_{3n+1}$, where $n=\infty$ for perovskites) have been objects of undying attention in the scientific community[9–11]. In the last years, this trend has been further accelerated by advances in defect engineering, which has improved the perspective of practical applications[8,12]. Despite their apparent simplicity, bulk materials exhibit a variety of ground states, driven by the strong interplay of different degrees of freedom[13–17]. The symmetry breaking at interfaces[18–21] leads to even more exciting phenomena, such as flat bands[22], anisotropic conductivity[23], magnetic anisotropy[24,25], exchange bias[26], spin-glass[27], electronic quantum confinement[28–30], unconventional superconductivity[31], topologically protected edge states[32,33], unexpected metallicity[34–38] and tunable quantum phase transitions[38–40].

Much research on interfaces and surfaces has been focused on mixed-valence manganites. Bulk materials are primarily known for their colossal magnetoresistance[41], which is favoured by a disordered solid mixture of Mn^{+3} and Mn^{+4} ions[42–44]. In superlattices, however, non trivial phenomena may be observed and ordered hetero-valent ions do not prevent the emergence of a large magnetoresistance[45]. Particularly studied are $(LaMnO_3)_n|(SrMnO_3)_m$ superlattices, where various magnetic and electronic ground states across the metal-insulator transition can be tuned[10,46–50]. This is achieved by varying their period $(n+m)$ or component ratio (n/m)[47,48,51], which is a way to modulate the tunnelling of e_g electrons across the interface[48]; orbital[52] and charge[53] order were also reported. More exotic phenomena, including correlated topological states, may be expected when passing from the (001) orientation to the (111) orientation, because of the large polarity and a peculiar symmetry-driven epitaxial strain[54,55]. This is the reason why (111)-oriented superlattices remain under intense scrutiny, despite of the scarcity of suitable substrates and unfavourable thermodynamics[55–57].

In this context, the current article presents an ab-initio study on the structural, electronic and magnetic properties of a (111)-oriented $(LaMnO_3)_{12}|(SrMnO_3)_6$ superlattice as illustrated in Fig. 1(a), which is isostochiometric to the colossal magnetoresistive $La_{2/3}Sr_{1/3}MnO_3$. Our calculations will show that this superlattice has a half-metallic ferromagnetic (FM) ground state, whose character persists inside the innermost layers of the component regions. This behaviour is profoundly different from what reported for other orientations and is traced back to the cooperation of charge transfer across the interface, strain, structural distortions and electronic correlations. Magnetism will be shown to originate from a double-exchange interaction between the Mn atoms and to be pinned inside the $LaMnO_3$ region and not at the interface. Finally, the Mott-Hund character of the electronic correlations will also be analysed.

RESULTS AND DISCUSSION

Ground-state structure and spectral properties

The $(LaMnO_3)_{12}|(SrMnO_3)_6$ superlattice is investigated via density functional theory (DFT) plus Hubbard U approach, labelled as sDFT+U. While tilting systems and angles are known for many perovskites in the bulk, their determination at surfaces and interfaces is not trivial. A previous ab-initio study[54] predicted that (111)-oriented manganite superlattices should adopt the $a^-a^-a^-$ tilting system instead of the native $a^-a^-c^+$ tilting system, as expressed in Glazer notation[58], used throughout this paper. The energy difference between these two structures depends on the lattice parameters. With a lattice constant of 3.860 Å (hereby denoted as equilibrium or 0% strain), the $a^-a^-c^+$ tilting system is favoured by 7.6 meV per formula unit (f.u., i.e., a $AMnO_3$ unit, where A may be La or Sr) with respect to the $a^-a^-a^-$ tilting system. A reasonably small compressive strain may change this structural order, as recently

[1]Department of Physics and Institute of Quantum Convergence and Technology, Kangwon National University, Chuncheon 24341, Korea. [2]Asia Pacific Center for Theoretical Physics, Pohang 37673, Korea. [3]Department of Physics and Astronomy, Uppsala University, Box 516, SE-75120 Uppsala, Sweden. [4]Department of Physics, POSTECH, Pohang 37673, Korea. ✉email: heungsikim@kangwon.ac.kr; igor.dimarco@apctp.org

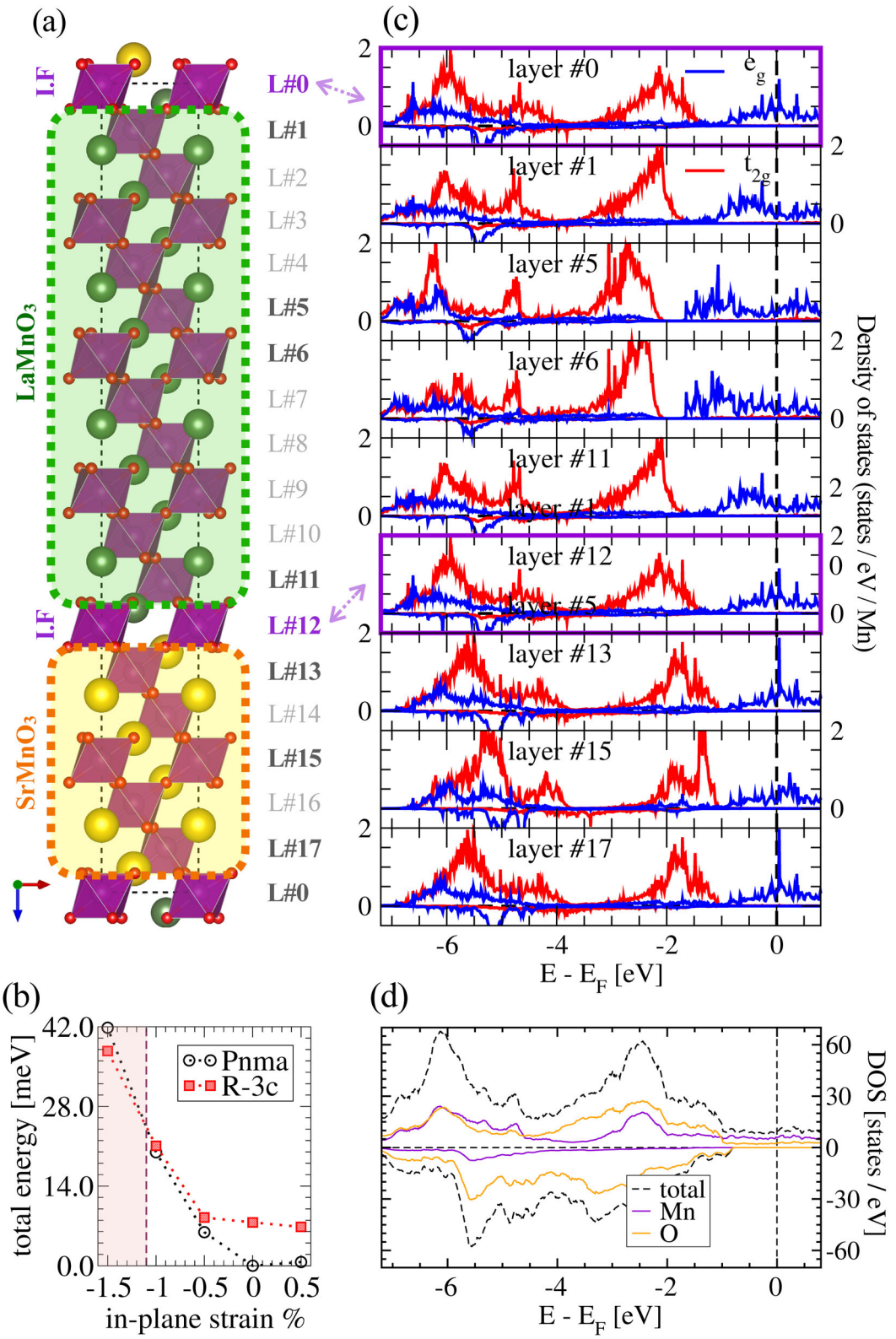

Fig. 1 Overview of the superlattice and its properties. a Crystal structure of the superlattice. The interfacial layers are #0 and #12. **b** Curve total energy vs strain for FM solutions with $a^-a^-c^+$ (black) and $a^-a^-a^-$ (red); `zero' strain means that the pseudo-cubic lattice constant is 3.860 Å. **c** Projected DOS for Mn-t_{2g} and Mn-e_g states for selected layers; additional information, covering all Mn and O layers, is provided in the Supplemental Material. **d** Total, Mn-*d* projected and O-*p* projected DOS for the FM solution.

Table 1. Energy difference per formula unit relative to the ground state structure – i.e., the FM phase with the $a^-a^-c^+$ tilting system – of various magnetic orders and tilting systems. The energies are computed for the same in-plane lattice parameters, corresponding to 0% strain.

	$a^-a^-c^+$	$a^-a^-a^-$
FM	G. S.	7.6
A-type AFM	26.5	37.5
C-type AFM	43.7	53.8
G-type AFM	71.8	95.6

reported for nickelates[59]. As shown in Fig. 1(b), we predict a transition to the $a^-a^-a^-$ tilting system for a compressive strain of ~ 1.5 %, corresponding to epitaxial growth on $SrMnO_3$ (on $LaAlO_3$ the strain is~2%). The energy difference between the two tilting systems remains below 7 meV (~80 K) at all simulated strain values, whereas that between the ground state FM and anti-ferromagnetic (AFM) orders are larger than 25 meV (~290 K), see Table 1. Therefore, phase transitions and coexistence are more likely to occur in the structure than in the magnetic order.

The two tilting systems do not lead to qualitatively different results in terms of distribution of charges and magnetic moments, but the $a^-a^-c^+$ requires a large supercell, which may hinder a thorough analysis of the layer-resolved properties. Therefore, we focus on the $a^-a^-a^-$ tilting system at the equilibrium lattice constant, for simplicity.

The superlattice analysed has a half-metallic character, as inferred by the total density of electronic states (DOS) in Fig. 1(d), with a band-gap in the minority-spin channel between Mn-*d* and O-*p* of ~2.0 eV. The site-projected DOS in Fig. 1(c) reveals that the half-metallicity persists across all the layers. The curves show that the deeper the Mn inside the $LaMnO_3$ region, the lower the onset of the e_g bands, because of the larger electronegativity of La with respect to Sr. The smooth variation of these onsets across the superlattice is a further signature of metallicity. Moreover, the e_g states are well separated from the t_{2g} states in the $LaMnO_3$ region (see layers 5 and 6), whereas they are much closer in the $SrMnO_3$ region. Their separation is small also at the interface, note the larger upshift of the t_{2g} states with respect to the e_g states in Fig. 1(b).

The features just outlined are unusual for manganite superlattices with this large thickness. For the (001) orientation, the superlattice becomes insulating if $LaMnO_3$ is thicker than 2 layers[48,53,60], whereas it is 12-layers thick in the present case. To understand the difference between the two orientations we should first understand what drives the formation of a half-metallic FM state. We recall that bulk $LaMnO_3$ (characterised by the $a^-a^-c^+$ tilting system) becomes half-metallic FM under a small compressive strain[61,62]. As discussed above, $SrMnO_3$ causes a small compressive strain on $LaMnO_3$, and this should be sufficient to induce the transition. Interestingly, this situation is even more favourable in the $a^-a^-a^-$ tilting system, which is predicted by our calculations to be a FM half-metal for all in-plane lattice parameters hereby considered.

Once established that strain is the driving factor in determining the half-metallic FM state in the $LaMnO_3$ region, we need to understand why this state is more likely to survive in the (111)-oriented superlattice than in its (001)-oriented counterpart. Clarifying this issue requires a deeper analysis of the structural features and the magnetic properties, presented in the next sections.

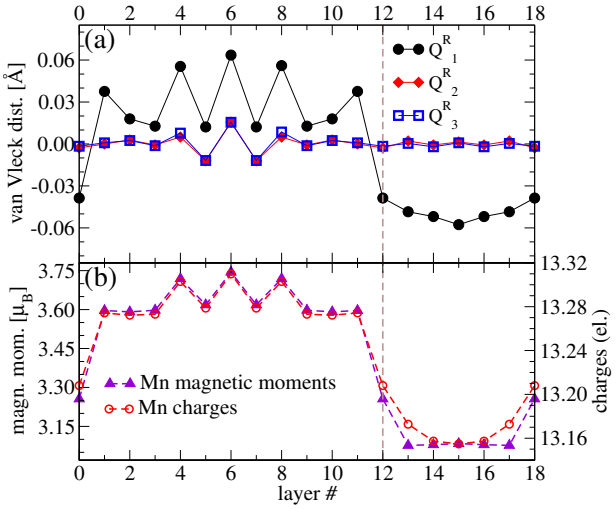

Fig. 2 Correlation between distortions and charge. a Layer-resolved van Vleck distortions. **b** Mn-projected Bader charges and magnetic moments. The dashed vertical line indicates the interfacial layer. The charge transfer across the interface is visible in having Bader charges larger (lower) than for the nominal oxidation state, i.e., 13 (14) in the SrMnO3 (LaMnO3) region. A more direct visualisation of the structure with respect to the layers numbering is provided in Fig. 1.

Breathing distortions and spin-charge oscillations

As for most perovskites, the structural features are linked to the electronic and magnetic properties. In agreement with leading literature[63,64], we introduce the Jahn-Teller distortions and breathing distortions in terms of the variations of the octahedral lengths *x*,*y*,*z* (with respect to their average values). Breathing distortions are defined as $Q_1^R = (\Delta x + \Delta y + \Delta z)/\sqrt{3}$, whereas the Jahn-Teller distortions are $Q_2^R = (\Delta x - \Delta y)/\sqrt{2}$ and $Q_3^R = (-\Delta x - \Delta y + 2\Delta z)/\sqrt{6}$. Breathing distortions are seldom found in manganites, which host orbital order and Jahn-Teller distortions (also defined in the Methods) instead. A recent study highlighted that Jahn-Teller modes arise from a steric effect that affects the electron-lattice coupling and are therefore dependent on the tilting system[65,66]. In the bulk, the constraint imposed by the $R\bar{3}c$ phase should lead to a total quenching of these (pseudo) Jahn-Teller modes. The Jahn-Teller distortions are shown in Fig. 2 (a) and are quenched in agreement with the aforementioned literature. The quenching is not full because the relaxation of the superlattice modifies the pristine $a^-a^-a^-$ tilting pattern.

The quenching of the Jahn-Teller modes is accompanied by the presence of the breathing modes. The latter are lessened by a factor 4 in the structure without tilts (data not shown). A similar relation between octahedral tilts and breathing distortions was recently found in rare-earth nickelates, where it leads to a structurally triggered metal-insulator transition[67]. In addition, $LaMnO_3$ is mentioned as a case where a close competition between charge and orbital order is driven by a similar mechanism (in line with refs. [63] and[68]). In the superlattice under investigation, this mechanism has to compete with the high stability of the FM half-metallic phase, associated to the strained structure, and with the uniform shift of the band-edge, induced by the charge transfer – see again Fig. 1(b). Therefore, it becomes unfavourable to induce a transition to an AFM insulator with orbital order. The site-projected charge and magnetic moment distributions, as computed *à la* Bader[69–73], is presented in Fig. 2(b) and shows a hint of charge order, leading to oscillations in the $LaMnO_3$ region and a smooth behaviour in the $SrMnO_3$ region.

The smooth variation of the Mn-O-Mn angles across the superlattice (which take approximately the same values for all

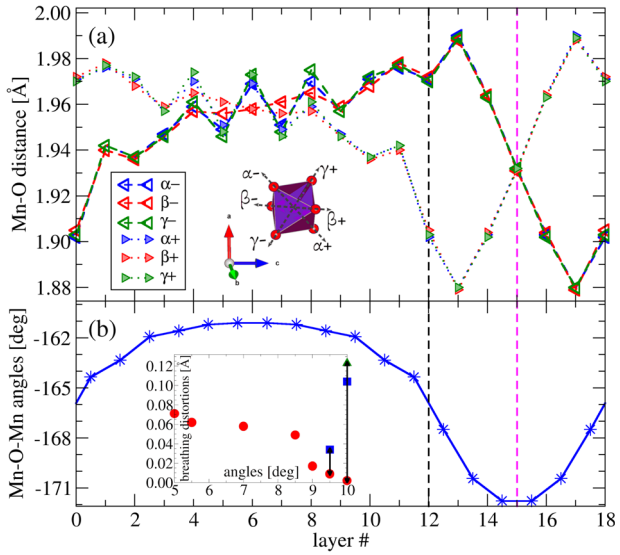

Fig. 3 Correlation between angles and distances/distortions. **a** Mn-O distance for the 3 inequivalent nearest neighbours, as illustrated in the inset; + and − denote increasing and decreasing *c*, respectively. **b** Opposite of the Mn-O-Mn angles ($\widehat{MnOMn}$) averaged over the three directions; inset: correlation between the angles $(\pi - \widehat{MnOMn})/2$ and the breathing distortions. In the main panels, the vertical dashed black line denotes the layer at the interface, while the dashed magenta line denotes the center of the $SrMnO_3$ region. Note that layers #0 and #18 are also at the interface. In the inset of panel (**b**), the vertical lines denote the range of breathing distortions for one corresponding value of the angle.

layers in the central $LaMnO_3$ region) mirrors the uniform shift of the band-edge, compare Figs. 3(b) and 1(b), whereas the Mn-O distances appear with oscillations in the inner $LaMnO_3$ region, see Fig. 3(a). Where the Mn-O-Mn bond are closer to a flat angle (the $SrMnO_3$ region) the structure presents larger splitting in the Mn-O distances between increasing $\hat{z}$ and decreasing $\hat{z}$, and where the Mn-O-Mn bonds are more bent (the $LaMnO_3$ region) the structure presents oscillating Mn-O distances and breathing modes, see Figs. 2, 3. In fact, the connection between breathing distortions and angles is even more apparent in the inset of Fig. 3(b), where flat angles correspond to single values for the MnO_6 volumes (breathing distortion) and bent angles – in the $LaMnO_3$ region – correspond to large variance of the MnO_6 volumes distribution, in line with the above mentioned literature[67]. The large Mn-O distance splitting, occurring in the $SrMnO_3$ region, reveals a typical tendency for $SrMnO_3$ to ferroelasticity[74], avoided by the symmetry with respect to the interface.

Exchange couplings and ferromagnetic order

As we argued that the magnetism is a consequence of structure and strain, we do not expect it to be interfacially driven. This is clearly visible in Fig. 2(b), where the largest magnetisation is found in the innermost layers of the $LaMnO_3$ region. For a better insight into the magnetic properties, we analyse the inter-atomic exchange coupling, computed for a lattice constant of 3.892 Å (which corresponds to a tensile strain below 1%). The largest contributions in the Mn sublattice are those connecting a Mn atom to its first nearest neighbours or fourth-nearest neighbours. The latter correspond to the second-nearest neighbours along Mn-O-Mn⋯ lines, consistently with the double-exchange mechanism[48,60]. The relevant exchange couplings across the superlattice are illustrated in Fig. 4. In the $LaMnO_3$ region, the magnetic order is driven by the FM nearest neighbour coupling, which in the innermost layer takes the value of 17.7 meV and sharply decreases at the interface, exhibiting oscillations in phase with the magnetic moments. Interestingly, the maximum value is not reached at the innermost layer, but at intermediate layers, and amounts to 18.4 meV, which is 30% smaller than in the isostochiometric $La_{2/3}Sr_{1/3}MnO_3$[75]. This behaviour reflects a competition between the trend of the magnetisation – see Fig. 2(b) – and the potential induced by the charge transfer across the interface – see Fig. 1(b). Such relatively strong ferromagnetism is even more surprising if compared to the behaviour of (001)-oriented supercells, whose nearest neighbour exchange becomes bulk-like AFM for $LaMnO_3$ regions thicker than 2 unit cells[48,60]. A smaller contribution to the magnetic order is given by the fourth-nearest neighbour exchange, whose values are noticeable at the interface (1.36 meV), but are totally quenched in the innermost layers of the $LaMnO_3$ region.

The situation is more complicated in the $SrMnO_3$ region. In the innermost layers, the nearest neighbour exchange is AFM, as in the bulk[76]. However, The strength of the coupling is much weaker than in the bulk, i.e., -1.6 meV versus -7.5meV[77], due to the combined effect of charge transfer and epitaxial strain (about 1%). Strain alone was shown to induce an AFM-FM transition at about 3% in bulk cubic $SrMnO_3$[77] – while here the strain is virtually null on $SrMnO_3$. Interestingly, the FM order inside the $SrMnO_3$ region is stabilised by the fourth-nearest neighbour coupling, which becomes even larger (1.8 meV) than the nearest neighbour one. This frustration due to competing FM and AFM interactions is likely to lead to a more complex magnetic structure, probably accompanied by non-collinearity. Exploring the magnetic phase diagram may be an interesting project, but outside the scope of the present work. We prefer, instead, to focus on the origin of the oscillations of charge, magnetic moments, exchange couplings and breathing distortions.

We can summarise what leads to the half-metallic FM state with the help of Fig. 5. In the bulk, $LaMnO_3$ and $SrMnO_3$ behave as an AFM Mott insulator with Mn^{3+} ions and an AFM band insulator with Mn^{+4} ions, respectively. In the superlattice, the local strain in the $LaMnO_3$ region induces the delocalisation of the Mn-3d states, which in turn suppresses the AFM super-exchange and favours the FM double-exchange[60,61]. This effect is further enhanced by the charge transfer across the interface, which penalises the ionic picture and promotes the hopping between Mn sites. In (001)-oriented superlattices, the local strain is imposed in-plane – hence along two crystallographic directions – and allows different relaxations in different regions: $SrMnO_3$ recovers its G-type AFM order, blocking the tunnelling of e_g electrons from $LaMnO_3$ and imposing a strong penalty on the double-exchange mechanism. For the (111) orientation, the strain acts on the same footing for all octahedral axes, and therefore the aforementioned phase separation is forbidden, the e_g tunnelling survives and the FM coupling prevails. In summary, geometrical degrees of freedom affect the electronic ones, governing the magnetic and metallic properties of the superlattice. Further information can be inferred by the analysis of the bond angles, shown in Fig. 3. In the $LaMnO_3$ region, the Mn-O-Mn angles vary from 160° to 165°. These values are higher than the bulk $LaMnO_3$[78] value of 155° and close to the $La_{2/3}Sr_{1/3}MnO_3$ value[79] of 165°. The analysis of the Mn-O bond lengths, see Fig. 3, is in line with the presence of breathing modes in the $LaMnO_3$, but also with a tendency to ferroelasticity in $SrMnO_3$, avoided by the equivalence of the interfaces. Such behaviour is typical of $SrMnO_3$[74]. Charge doping and metallicity would anyway prevent the transition to a ferroelectric phase.

Role of Hund's coupling

The suppression of Jahn-Teller order in favour of breathing distortions was predicted a decade ago in nickelates as a consequence of Hund's coupling and was pointed out to be persistent well into the metallic side of the Mott transition[80].

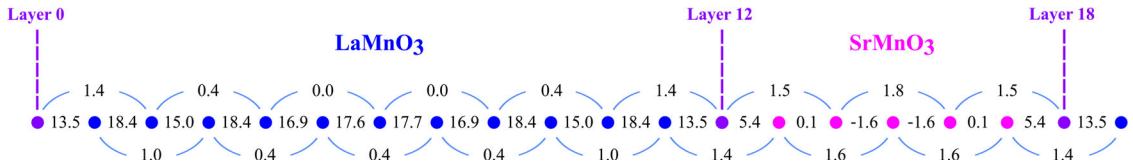

Fig. 4 Magnetic coupling constants as computed and shown along the (001) – or any of the equivalent (010) and (100) – crystallographic directions of the superlattice. The Mn are shown as circles, and the values of the coupling constants are reported in meV. Straight segments denote first nearest neighbours, whereas semicircles denote fourth-nearest neighbours, namely Mn two layers away but along the same Mn-O-Mn direction (whereas they vanish for all other Mn couples).

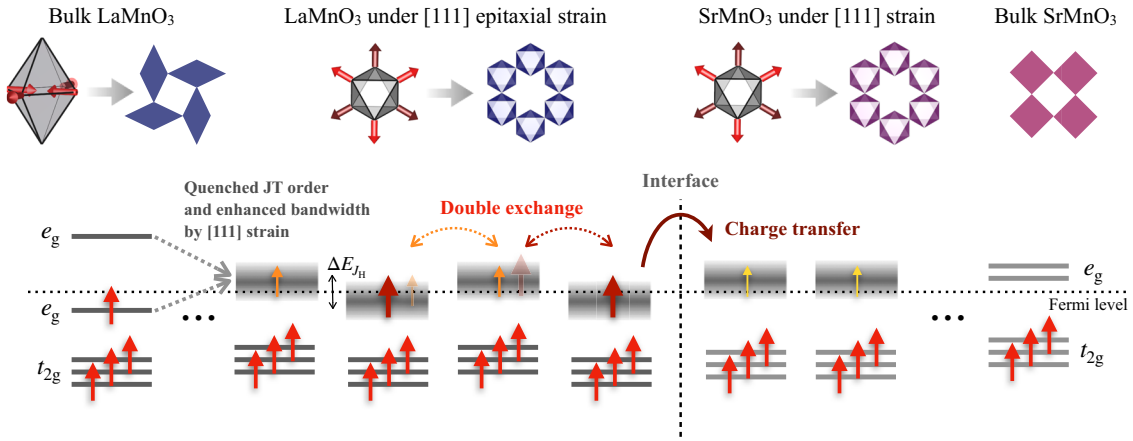

Fig. 5 Sketch of the physical mechanisms driving the interface behaviour in the superlattice. Bulk $LaMnO_3$ (left side) is an AFM Mott insulator with Jahn-Teller distortion and orbital order, in a d^4 ionic configuration. Bulk $SrMnO_3$ (right side) is an AFM band insulator in a d^3 configuration. Across the interface, charge transfer and epitaxial strain lead to partially filled bands and breathing distortions, while the Jahn-Teller order is quenched. Metallicity favours the FM order driven by the double-exchange mechanism, and in turn accompanied by spin and charge oscillations.

Later studies[67] pointed to structural distortions as the driving mechanism. In the present case, we observe an intermediate situation. On one hand, the structure has a primary importance, forbidding certain distortions, such as Jahn-Teller, and preserving metallicity. On the other hand, the breathing distortions are not large enough to induce a metal-insulator transition, but we still observe signs of charge order. The dependence of our results on the strength of Hund's exchange J is investigated via charge density functional plus U scheme (denoted as cDFT+U|J hereafter)[81,82] for a lattice constant of 3.892 Å. It suggests to what extent Hund's coupling affects the properties of our system. The oscillations of the magnetic moments across the superlattice depend crucially on the value of Hund's coupling, see Fig. 6(b). When J becomes as small as 0.6 eV, the magnetism is no longer pinned at the innermost layers of the $LaMnO_3$ region. Instead, it becomes pinned at the interface, similarly to what happens in (001)-oriented superlattices. The change in the trend of the magnetic moments across the superlattice is accompanied by an analogous change of the breathing distortions, emphasising that the former drives the latter, to a large extent. Furthermore, electron/hole doping may lead to the disappearance of the breathing distortions as well as the magnetic moments oscillations (data not shown). Such a drastic change is surprising, considering the shape of the density of states in the corresponding doping range (± 0.1 eV), and suggests that strong electronic correlations play an important role. Overall, the metallic character with spin and charge oscillations, the presence of strong correlation effects, and the key role of the Hund's exchange J suggest that our superlattice behaves as a Hund's metal[83,84]. Using our parameters U and J, as well as the effective bandwidth extracted from the DOS, we can obtain some information from existing phase diagrams of the Hubbard model[85–87]. The most accurate comparison is offered by ref. [87], where Merkel et al. investigated

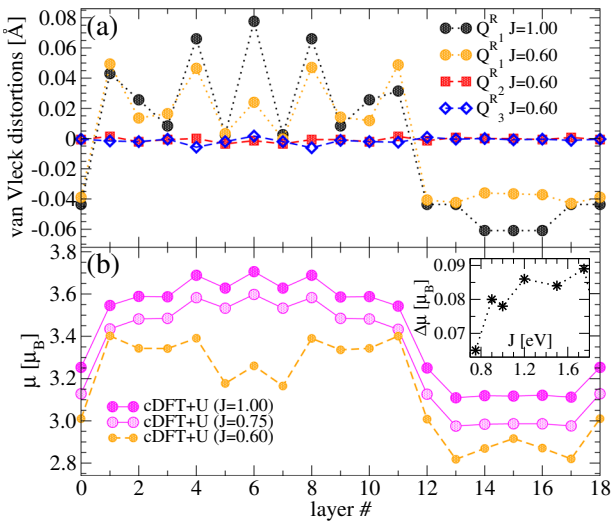

Fig. 6 Dependence of the distortions and charge/spin distribution on the correlation. a Layer-resolved van Vleck distortions and (**b**) Mn-projected Bader magnetic moments for different values of Hund's exchange J (in eV). See the Methods section for details on cDFT+U|J and sDFT+U|J. Inset: difference $\Delta\mu$ between the magnetic moments at layers #5 and #6, which provides a measure of the amplitude of the moment oscillations.

a 5 orbital system with a d^4 occupation, including the level splittings associated to the presence of breathing modes (representative of $CaFeO_3$). Using their phase diagram, we can confirm the regime of (homogeneous) Hund's metallicity, with an

estimated quasiparticle weight between 0.4 and 0.6. By increasing J, we expect to get closer to a valence skipping metal phase, which finds correspondence in an increasing amplitude of charge and spin oscillations (see inset of Fig. 6(b)). A further increase of J would lead to a charge disproportionated insulator, which in ref. [87] is predicted to happen for values larger than 2.3 eV. Despite signs of "Hundness" have been found in a variety of systems during the last decade[83,84], they had never been reported for a manganite superlattice. For a more quantitative analysis allowing for more precise conclusions, one would need to perform calculations beyond DFT, e.g., in combination with the dynamical mean-field theory (DMFT), including the structural response. Considering the size of the system as well as the very high number of degrees of freedom, such an analysis would be beyond the scope of the present study.

Outlook

In summary, we have investigated the electronic and magnetic properties of the (111)-oriented $(LaMnO_3)_{12}|(SrMnO_3)_6$ superlattice using DFT+U|J. A half-metallic FM state is supported by the cooperation of charge, spin, orbital and lattice degrees of freedom, and is favoured with respect to an AFM state. The half-metallic FM character is found to persist across the entire superlattice, while the innermost layers of its (001)-oriented counterpart become AFM insulators for a thickness larger than 3 layers. The atomic volumes, charges and magnetic moments are correlated across the superlattice, in particular in the $LaMnO_3$ region, where adjacent sites display charge, spin, and volume oscillations. Breathing distortions arise and may be accompanied by the quenching of Jahn-Teller distortions in the presence of $a^-a^-a^-$ tilting of MnO_6 octahedra while may coexist with the Jahn-Teller distortions in other tilting systems such as $a^-a^-c^+$. Overall, the present results suggest that the [111] epitaxial strain associated to the superlattice formation is a viable pathway to engineer a system analogous to $La_{2/3}Sr_{1/3}MnO_3$ without introducing doping-induced disorder. This is not only an advantage for avoiding alloy-related problems, as e.g. cation disorder, but does also widen the potential of interfacial engineering in oxide heterostructures. Finally, we also speculate that the fascinating physics exhibited by this superlattice may arise from Hundness, alongside with structural aspects, similarly to what happens in nickelates. Therefore, the system addressed here can provide further theoretical ground for the development of heterostructures hosting exotic magnetic phases and topological states.

METHODS

Framework and parameters

The superlattice is fully relaxed with an optimised lattice constant of 3.860 Å (denoted as equilibrium or 0 % strain). Calculations are performed in density functional theory (DFT) using the projector-augmented wave method as implemented in the Vienna Ab-initio Simulation Package (VASP)[88,89]. The exchange-correlation functional is treated in the generalised gradient approximation (GGA) by Perdew-Burke-Ernzerhof[90,91]. To improve the description of the Mn-3d states[92], we make use of on-site corrections for static correlation effects in the rotational invariant DFT+U approach by Liechtenstein et al.[93], denoted as sDFT+U|J. Further calculations to analyse Hund's coupling are performed by following the approach discussed in ref. [94], which we label as cDFT+U|J. The Coulomb interaction parameters are chosen as $U = 3.8$ eV and $J = 1.0$ eV, in accordance with works on similar systems[95,96]. A deeper analysis of the magnetic properties is then performed via the full-potential linear muffin-tin orbital (FP-LMTO) method as implemented in the RSPt code[97–99]. We used also the SCAN parameter-free functional[100]: results (shown in the Supplemental Material) confirm the core results obtained with DFT+U|J.

The inter-atomic exchange interactions J_{ij} are calculated by mapping the magnetic excitations onto an effective Heisenberg Hamiltonian $\hat{H} = -\sum_{i \neq j} J_{ij} \cdot (\vec{e}_i \cdot \vec{e}_j)$, where i, j are atomic sites and $\vec{e}_i$, $\vec{e}_j$ are unit vectors along the local magnetisation direction. This calculation is performed via the magnetic force theorem, using the implementation of ref. [101], which was also successfully applied to CaMnO3[21]. Due to the better accuracy of all-electron methods[102], these calculations also serve to confirm the validity of VASP results.

General considerations on the modelled system

The supercells used for the calculations consist of two types: the $R\bar{3}c$ cell was used for the results presented throughout this work, whereas an orthorhombic cell was used for calculations to compare total energies and results on the charge and spin distributions. The two interfaces have the same stacking sequence (i.e., $LaO_3|Mn|SrO_3$ or $SrO_3|Mn|LaO_3$), thus they are equivalent; furthermore, the superlattice possess inversion symmetry with respect to the Mn atom at the interface and therefore there is no built-in electric field generated. Further details on the cells and the sampling of the Brillouin zones are given in the Supplemental Material.

The analysis on the on-site charges and magnetic moments is carried on by in agreement with state-of-the-art methods[69–73]. The analysis of the electronic properties is performed with the aid of the post-processing code VASPKIT[103]. Finally, images of structures and charge/spin distributions are produced with VESTA JP-Minerals[104]. Further details on the calculations are given in the Supplemental Material.

DATA AVAILABILITY

The datasets generated during and/or analysed during the current study are available from the first author on reasonable request.

CODE AVAILABILITY

The calculations for this work have been performed with VASP and RSPt. The former is a licence product from the University of Vienna; the licence can be obtained upon submitting an application through the vasp portal (http://www.vasp.at). The latter is a free software distributed under GPL license after registration to a mailing list. More information about RSPt can be found at http://fplmto-rspt.org/[98].

Received: 6 August 2021; Accepted: 23 March 2022;
Published online: 21 April 2022

REFERENCES

1. Prakash, A. & Jalan, B. Molecular beam epitaxy for oxide electronics. In *Molecular Beam Epitaxy: Materials and Applications for Electronics and Optoelectronics*. 423–452 (John Wiley & Sons Ltd, 2019).
2. Ismail-Beigi, S., Walker, F. J., Disa, A. S., Rabe, K. M. & Ahn, C. H. Picoscale materials engineering. *Nat. Rev. Mater.* **2**, 17060 (2017).
3. Christen, H. M. & Eres, G. Recent advances in pulsed-laser deposition of complex oxides. *J. Phys.: Condens. Matter* **20**, 264005 (2008).
4. Aruta, C. et al. Pulsed laser deposition of $SrTiO_3/LaGaO_3$ and $SrTiO_3/LaAlO_3$: Plasma plume effects. *Appl. Phys. Lett.* **97**, 252105 (2010).
5. Eres, G. et al. Dynamic scaling and island growth kinetics in pulsed laser deposition of $SrTiO_3$. *Phys. Rev. Lett.* **117**, 206102 (2016).
6. Yao, X., Schneider, C. W., Lippert, T. & Wokaun, A. Manipulation of ion energies in pulsed laser deposition to improve film growth. *Appl. Phys. A* **125**, 344 (2019).
7. Lorenz, M. Pulsed laser deposition. In *Digital Encyclopedia of Applied Physics*. 1–29 (John Wiley & Sons Ltd, 2019).
8. Koster, G., Blank, D. H. A. & Rijnders, G. A. J. H. M. Oxygen in complex oxide thin films grown by pulsed laser deposition: A perspective. *J. Supercond. Novel Magn.* **33**, 205–212 (2020).
9. Gao, X. et al. Ruddlesden-popper perovskites: Synthesis and optical properties for optoelectronic applications. *Adv. Sci.* **6**, 1900941 (2019).
10. Chen, H. & Millis, A. Charge transfer driven emergent phenomena in oxide heterostructures. *J. Phys.: Condens. Matter* **29**, 243001 (2017).
11. Righetto, M., Giovanni, D., Lim, S. S. & Sum, T. C. The photophysics of Ruddlesden-Popper perovskites: A tale of energy, charges, and spins. *Appl. Phys. Rev.* **8**, 011318 (2021).
12. Li, W., Shi, J., Zhang, K. H. L. & MacManus-Driscoll, J. L. Defects in complex oxide thin films for electronics and energy applications: Challenges and opportunities. *Mater. Horiz.* **7**, 2832–2859 (2020).
13. Dagotto, E. Complexity in strongly correlated electronic systems. *Science* **309**, 257–262 (2005).
14. Ngai, J., Walker, F. & Ahn, C. Correlated oxide physics and electronics. *Annu. Rev. Mater. Res.* **44**, 1–17 (2014).

15. Tokura, Y. & Nagaosa, N. Orbital physics in transition-metal oxides. *Science* **288**, 462–468 (2000).
16. Cheong, S.-W. The exciting world of orbitals. *Nat. Mater.* **6**, 927–928 (2007).
17. Schlom, D. G. et al. Elastic strain engineering of ferroic oxides. *MRS Bull.* **39**, 118–130 (2014).
18. Flint, C. L. et al. Enhanced interfacial ferromagnetism and exchange bias in (111)-oriented $LaNiO_3/CaMnO_3$ superlattices. *Phys. Rev. Mater.* **3**, 064401 (2019).
19. Grutter, A. J. et al. Interfacial symmetry control of emergent ferromagnetism at the nanoscale. *Nano. Lett.* **16**, 5647–5651 (2016).
20. Flint, C. L., Grutter, A. J., Jenkins, C. A., Arenholz, E. & Suzuki, Y. Magnetism in $CaMnO_3$ thin films. *J. Appl. Phys.* **115**, 17D712 (2014).
21. Keshavarz, S. et al. Exchange interactions of $CaMnO_3$ in the bulk and at the surface. *Phys. Rev. B* **95**, 115120 (2017).
22. Rüegg, A., Mitra, C., Demkov, A. A. & Fiete, G. A. Electronic structure of $(LaNiO_3)_2/(LaAlO_3)_N$ heterostructures grown along [111]. *Phys. Rev. B* **85**, 245131 (2012).
23. Annadi, A. et al. Anisotropic two-dimensional electron gas at the $LaAlO_3/SrTiO_3$ (110) interface. *Nat. Commun.* **4**, 1838 (2013).
24. Kim, B. & Min, B. I. Termination-dependent electronic and magnetic properties of ultrathin $SrRuO_3$ (111) films on $SrTiO_3$. *Phys. Rev. B* **89**, 195411 (2014).
25. Asaba, T. et al. Unconventional ferromagnetism in epitaxial (111) $LaNiO_3$. *Phys. Rev. B* **98**, 121105 (2018).
26. Gibert, M., Zubko, P., Scherwitzl, R., Íñiguez, J. & Triscone, J.-M. Exchange bias in $LaNiO_3$-$LaMnO_3$ superlattices. *Nat. Mater.* **11**, 195–198 (2012).
27. Huangfu, S. et al. Short-range magnetic interactions and spin-glass behavior in the quasi-two-dimensional nickelate $Pr_4iNi_3O_8$. *Phys. Rev. B* **102**, 054423 (2020).
28. Yoo, H. K. et al. Thickness-dependent electronic structure in ultrathin $LaNiO_3$ films under tensile strain. *Phys. Rev. B* **93**, 035141 (2016).
29. Liu, J. et al. Quantum confinement of Mott electrons in ultrathin $LaNiO_3/LaAlO_3$ superlattices. *Phys. Rev. B* **83**, 161102 (2011).
30. Dong, S. & Dagotto, E. Quantum confinement induced magnetism in $LaNiO_3$-$LaMnO_3$ superlattices. *Phys. Rev. B* **87**, 195116 (2013).
31. Li, D. et al. Superconductivity in an infinite-layer nickelate. *Nature* **572**, 624–627 (2019).
32. Doennig, D., Pickett, W. E. & Pentcheva, R. Massive symmetry breaking in $LaAlO_3/SrTiO_3$ (111) quantum wells: A three-orbital strongly correlated generalization of graphene. *Phys. Rev. Lett.* **111**, 126804 (2013).
33. Rüegg, A., Mitra, C., Demkov, A. A. & Fiete, G. A. Lattice distortion effects on topological phases in $(LaNiO_3)_2/(LaAlO_3)_N$ heterostructures grown along the [111] direction. *Phys. Rev. B* **88**, 115146 (2013).
34. Li, C. et al. The metallic interface between insulating $NdGaO_3$ and $SrTiO_3$ perovskites. *Appl. Phys. Lett.* **103**, - (2013).
35. Cossu, F., Schwingenschlögl, U., Colizzi, G., Filippetti, A. & Fiorentini, V. Surface antiferromagnetism and incipient metal-insulator transition in strained manganite films. *Phys. Rev. B* **87**, 214420 (2013).
36. Cossu, F., Jilili, J. & Schwingenschlögl, U. 2D electron gas with 100% spin-polarization in the $(LaMnO_3)_2/(SrTiO_3)_2$ superlattice under uniaxial strain. *Adv. Mater. Inter.* **1**, n/a-n/a (2014).
37. Zubko, P., Gariglio, S., Gabay, M., Ghosez, P. & Triscone, J.-M. Interface physics in complex oxide heterostructures. *Annu. Rev. Condens. Matter Phys.* **2**, 141–165 (2011).
38. Hwang, H. et al. Emergent phenomena at oxide interfaces. *Nat. Mater.* **11**, 103–113 (2012).
39. Marques, C. A. et al. Magnetic-field tunable intertwined checkerboard charge order and nematicity in the surface layer of Sr_2RuO_4. *Adv. Mater.* **33**, 2100593 (2021).
40. Pauli, S. A. & Willmott, P. R. Conducting interfaces between polar and non-polar insulating perovskites. *J. Phys.: Condens. Matter* **20**, 264012 (2008).
41. Imada, M., Fujimori, A. & Tokura, Y. Metal-insulator transitions. *Rev. Mod. Phys.* **70**, 1039–1263 (1998).
42. Burgy, J., Mayr, M., Martin-Mayor, V., Moreo, A. & Dagotto, E. Colossal effects in transition metal oxides caused by intrinsic inhomogeneities. *Phys. Rev. Lett.* **87**, 277202 (2001).
43. Dagotto, E. Open questions in CMR manganites, relevance of clustered states and analogies with other compounds including the cuprates. *New J. Phys.* **7**, 67–67 (2005).
44. Şen, C., Alvarez, G. & Dagotto, E. Competing ferromagnetic and charge-ordered states in models for manganites: The origin of the colossal magnetoresistance effect. *Phys. Rev. Lett.* **98**, 127202 (2007).
45. Nakao, H. et al. Magnetic and electronic states in $(LaMnO_3)_2(SrMnO_3)_2$ superlattice exhibiting a large negative magnetoresistance. *Phys. Rev. B* **92**, 245104 (2015).
46. Adamo, C. et al. Tuning the metal-insulator transitions of $(SrMnO_3)_n/(LaMnO_3)_{2n}$ superlattices: Role of interfaces. *Phys. Rev. B* **79**, 045125 (2009).
47. Bhattacharya, A. et al. Metal-insulator transition and its relation to magnetic structure in $(LaMnO_3)_{2n}/(SrMnO_3)_n$ superlattices. *Phys. Rev. Lett.* **100**, 257203 (2008).
48. Nanda, B. R. K. & Satpathy, S. Electronic and magnetic structure of the $(LaMnO_3)_{2n}/(SrMnO_3)_n$ superlattices. *Phys. Rev. B* **79**, 054428 (2009).
49. Smadici, S. et al. Electronic reconstruction at $SrMnO_3$-$LaMnO_3$ superlattice interfaces. *Phys. Rev. Lett.* **99**, 196404 (2007).
50. Dong, S. et al. Magnetism, conductivity, and orbital order in $(LaMnO_3)_{2n}/(SrMnO_3)_n$ superlattices. *Phys. Rev. B* **78**, 201102 (2008).
51. May, S. J. et al. Enhanced ordering temperatures in antiferromagnetic manganite superlattices. *Nat. Mater.* **8**, 892–897 (2009).
52. Nakao, H. et al. Charge disproportionation of Mn 3*d* and O 2*p* electronic states depending on strength of $p-d$ hybridization in $(LaMnO_3)_2/(SrMnO_3)_2$ superlattices. *Phys. Rev. B* **98**, 245146 (2018).
53. Pardo, V., Botana, A. S. & Baldomir, D. Charge ordering at the interface in $(LaMnO_3)_{2n}/(SrMnO_3)_n$ superlattices as the origin of their insulating state. *Appl. Phys. Lett.* **104**, - (2014).
54. Cossu, F., Tahini, H. A., Singh, N. & Schwingenschlögl, U. Charge driven metal-insulator transitions in $LaMnO_3|SrTiO_3$ (111) superlattices. *EPL (Europhys. Lett.)* **118**, 57001 (2017).
55. Chakhalian, J., Liu, X. & Fiete, G. A. Strongly correlated and topological states in [111] grown transition metal oxide thin films and heterostructures. *APL Mater.* **8**, 050904 (2020).
56. Mastrikov, Y., Heifets, E., Kotomin, E. & Maier, J. Atomic, electronic and thermodynamic properties of cubic and orthorhombic $LaMnO_3$ surfaces. *Surf. Sci.* **603**, 326–335 (2009).
57. Mantz, Y. A. New $LaMnO_3$ surface energy results obtained from density-functional theory. *Surf. Sci.* **695**, 121500 (2020).
58. Glazer, A. M. The classification of tilted octahedra in perovskites. *Acta. Crystallogr. Sect. B* **28**, 3384–3392 (1972).
59. Kim, J. R. et al. Stabilizing hidden room-temperature ferroelectricity via a metastable atomic distortion pattern. *Nat. Commun.* **11**, 4944 (2020).
60. Bhattacharya, A. & May, S. J. Magnetic oxide heterostructures. *Annu. Rev. Mater. Res.* **44**, 65–90 (2014).
61. Lee, J. H., Delaney, K. T., Bousquet, E., Spaldin, N. A. & Rabe, K. M. Strong coupling of Jahn-Teller distortion to oxygen-octahedron rotation and functional properties in epitaxially strained orthorhombic $LaMnO_3$. *Phys. Rev. B* **88**, 174426 (2013).
62. Rivero, P., Meunier, V. & Shelton, W. Uniaxial pressure-induced half-metallic ferromagnetic phase transition in lamno$_3$. *Phys. Rev. B* **93**, 094409 (2016).
63. Schmitt, M. M., Zhang, Y., Mercy, A. & Ghosez, P. Electron-lattice interplay in $LaMnO_3$ from canonical Jahn-Teller distortion notations. *Phys. Rev. B* **101**, 214304 (2020).
64. Van Vleck, J. H. The Jahn-Teller effect and crystalline stark splitting for clusters of the form XY_6. *J. Chem. Phys.* **7**, 72–84 (1939).
65. Varignon, J., Bibes, M. & Zunger, A. Mott gapping in 3*d*-ABO_3 perovskites without Mott-Hubbard interelectronic repulsion energy U. *Phys. Rev. B* **100**, 035119 (2019).
66. Varignon, J., Bibes, M. & Zunger, A. Origins versus fingerprints of the Jahn-Teller effect in *d*-electron $AB{X}_3$ perovskites. *Phys. Rev. Res.* **1**, 033131 (2019).
67. Mercy, A., Bieder, J., Íñiguez, J. & Ghosez, P. Structurally triggered metal-insulator transition in rare-earth nickelates. *Nat. Commun.* **8**, 1677 (2017).
68. Varignon, J., Bibes, M. & Zunger, A. Origin of band gaps in 3d perovskite oxides. *Nat. Commun.* **10**, 1658 (2019).
69. Tang, W., Sanville, E. & Henkelman, G. A grid-based bader analysis algorithm without lattice bias. *J. Phys.: Cond. Matter* **21**, 084204 (2009).
70. Sanville, E., Kenny, S. D., Smith, R. & Henkelman, G. Improved grid-based algorithm for bader charge allocation. *J. Comput. Chem.* **28**, 899–908 (2007).
71. Henkelman, G., Arnaldsson, A. & Jónsson, H. A fast and robust algorithm for bader decomposition of charge density. *Comput. Mater. Sci.* **36**, 354–360 (2006).
72. Yu, M. & Trinkle, D. R. Accurate and efficient algorithm for bader charge integration. *J. Chem. Phys.* **134**, 064111 (2011).
73. https://github.com/adam-kerrigan/bader-rs/releases/tag/v0.4.0.
74. Marthinsen, A., Faber, C., Aschauer, U., Spaldin, N. A. & Selbach, S. M. Coupling and competition between ferroelectricity, magnetism, strain, and oxygen vacancies in $AMnO_3$ perovskites. *MRS Commun.* **6**, 182–191 (2016).
75. Furrer, A., Podlesnyak, A., Pomjakushina, E. & Pomjakushin, V. Effect of sr doping on the magnetic exchange interactions in manganites of type $La_{1-x}Sr_xMn_yA_{1-y}O_3$ (A = Ga,Ti;$0.1 \le y \le 1$). *Phys. Rev. B* **95**, 104414 (2017).
76. Ricca, C., Timrov, I., Cococcioni, M., Marzari, N. & Aschauer, U. Self-consistent site-dependent DFT+*U* study of stoichiometric and defective $SrMnO_3$. *Phys. Rev. B* **99**, 094102 (2019).
77. Zhu, X., Edström, A. & Ederer, C. Magnetic exchange interactions in $SrMnO_3$. *Phys. Rev. B* **101**, 064401 (2020).
78. Jilili, J., Cossu, F. & Schwingenschlögl, U. Trends in $(LaMnO_3)_n/(SrTiO_3)_m$ superlattices with varying layer thicknesses. *Sci. Rep.* **5**, 13762 (2015).
79. Colizzi, G., Filippetti, A., Cossu, F. & Fiorentini, V. Interplay of strain and magnetism in $La_{1-x}Sr_xMnO_3$ from first principles. *Phys. Rev. B* **78**, 235122 (2008).
80. Mazin, I. I. et al. Charge ordering as alternative to Jahn-Teller distortion. *Phys. Rev. Lett.* **98**, 176406 (2007).
81. Keshavarz, S., Schött, J., Millis, A. J. & Kvashnin, Y. O. Electronic structure, magnetism, and exchange integrals in transition-metal oxides: Role of the spin

polarization of the functional in DFT+U calculations. *Phys. Rev. B* **97**, 184404 (2018).
82. Jang, S. W., Ryee, S., Yoon, H. & Han, M. J. Charge density functional plus u theory of $LaMnO_3$: Phase diagram, electronic structure, and magnetic interaction. *Phys. Rev. B* **98**, 125126 (2018).
83. Georges, A., Medici, L. D. & Mravlje, J. Strong correlations from hund's coupling. *Ann. Rev. Cond. Matter Phys.* **4**, 137–178 (2013).
84. Stadler, K., Kotliar, G., Weichselbaum, A. & von Delft, J. Hundness versus Mottness in a three-band Hubbard-Hund model: On the origin of strong correlations in Hund metals. *Annals Phys.* **405**, 365–409 (2019).
85. Fanfarillo, L. & Bascones, E. Electronic correlations in Hund metals. *Phys. Rev. B* **92**, 075136 (2015).
86. Isidori, A. et al. Charge disproportionation, mixed valence, and Janus effect in multiorbital systems: A tale of two insulators. *Phys. Rev. Lett.* **122**, 186401 (2019).
87. Merkel, M. E. & Ederer, C. Charge disproportionation and hund's insulating behavior in a five-orbital hubbard model applicable to d^4 perovskites. *Phys. Rev. B* **104**, 165135 (2021).
88. Kresse, G. & Furthmüller, J. Efficient iterative schemes for ab initio total-energy calculations using a plane-wave basis set. *Phys. Rev. B* **54**, 11169–11186 (1996).
89. Kresse, G. & Joubert, D. From ultrasoft pseudopotentials to the projector augmented-wave method. *Phys. Rev. B* **59**, 1758–1775 (1999).
90. Perdew, J. P., Burke, K. & Ernzerhof, M. Generalized gradient approximation made simple. *Phys. Rev. Lett.* **77**, 3865–3868 (1996).
91. Perdew, J. P., Burke, K. & Ernzerhof, M. Generalized gradient approximation made simple. *Phys. Rev. Lett.* **78**, 1396–1396 (1997).
92. Mellan, T. A., Corà, F., Grau-Crespo, R. & Ismail-Beigi, S. Importance of anisotropic coulomb interaction in $LaMnO_3$. *Phys. Rev. B* **92**, 085151 (2015).
93. Liechtenstein, A. I., Anisimov, V. I. & Zaanen, J. Density-functional theory and strong interactions: Orbital ordering in Mott-Hubbard insulators. *Phys. Rev. B* **52**, R5467–R5470 (1995).
94. Park, H., Millis, A. J. & Marianetti, C. A. Density functional versus spin-density functional and the choice of correlated subspace in multivariable effective action theories of electronic structure. *Phys. Rev. B* **92**, 035146 (2015).
95. Nanda, B. R. K. & Satpathy, S. Polar catastrophe, electron leakage, and magnetic ordering at the $LaMnO_3/SrMnO_3$ interface. *Phys. Rev. B* **81**, 224408 (2010).
96. Nanda, B. R. K. & Satpathy, S. Spin-polarized two-dimensional electron gas at oxide interfaces. *Phys. Rev. Lett.* **101**, 127201 (2008).
97. Wills, J. M. et al. Full-potential electronic structure method. electronic structure and physical properties of solids: Springer series in solid-state sciences (Springer-Verlag, Berlin, 2010).
98. http://fplmto-rspt.org.
99. Grånäs, O. et al. Charge self-consistent dynamical mean-field theory based on the full-potential linear muffin-tin orbital method: Methodology and applications. *Comput. Mater. Sci.* **55**, 295–302 (2012).
100. Sun, J., Ruzsinszky, A. & Perdew, J. P. Strongly constrained and appropriately normed semilocal density functional. *Phys. Rev. Lett.* **115**, 036402 (2015).
101. Kvashnin, Y. O. et al. Exchange parameters of strongly correlated materials: Extraction from spin-polarized density functional theory plus dynamical mean-field theory. *Phys. Rev. B* **91**, 125133 (2015).
102. Lejaeghere, K. et al. Reproducibility in density functional theory calculations of solids. *Science.* **351**, aad3000 (2016).
103. Wang, V., Xu, N., Liu, J. C., Tang, G. & Geng, W.-T. Vaspkit: A user-friendly interface facilitating high-throughput computing and analysis using vasp code (2019). arXiv:1908.08269.
104. Momma, K. & Izumi, F. *VESTA3* for three-dimensional visualization of crystal, volumetric and morphology data. *J. Appl. Crystallogr.* **44**, 1272–1276 (2011).

ACKNOWLEDGEMENTS

We acknowledge the support of computational resources, including technical assistance, from the Swedish National Infrastructure for Computing (SNIC) at the National Supercomputer Centre (NSC) of Linköping University (Sweden) and at the High Performance Computing Centre North (HPC2N), partially funded by the Swedish Research Council through grant agreement no. 2018-05973, as well as from the National Supercomputing Center of Korea (Grant No. KSC-2020-CRE-0156). F. C. acknowledges financial support from the National Research Foundation (NRF) funded by the Ministry of Science of Korea (Grant No. 2017R1D1A1B03033465). NRF support is also acknowledged by F. C. and H.-S. K. for the Basic Science Research Program, Grant No. 2020R1C1C1005900, and by I. D. M. for the Mid-Career Grant No. 2020R1A2C101217411. I. D. M. acknowledges also financial support from the European Research Council (ERC), Synergy Grant FASTCORR, Project No. 854843. The work of I. D. M. is supported by the appointment to the JRG program at the APCTP through the Science and Technology Promotion Fund and Lottery Fund of the Korean Government, as well as by the Korean Local Governments, Gyeongsangbuk-do Province and Pohang City. The authors, in particular F. C., are also grateful to Hassan A. Tahini and Adam M. Kerrigan for substantial scientific discussions and technical support.

AUTHOR CONTRIBUTIONS

F. C. planned the project and performed all the VASP calculations. I. D. M. performed all the RSPt calculations. F. C. and I. D. M. wrote the initial paper. All authors contributed to analysing the data, revising the paper and drawing the conclusions.

COMPETING INTERESTS

The authors declare no competing interests.

ADDITIONAL INFORMATION

Supplementary information The online version contains supplementary material available at https://doi.org/10.1038/s41524-022-00759-x.

Correspondence and requests for materials should be addressed to Heung-Sik Kim or Igor Di Marco.

Reprints and permission information is available at http://www.nature.com/reprints

Publisher's note Springer Nature remains neutral with regard to jurisdictional claims in published maps and institutional affiliations.